AMERICAN SOCIETY FOR MICROBIOLOGY | mBio

Check for updates

| Host-Microbial Interactions | Research Article

The *Bordetella* effector protein BteA induces host cell death by disruption of calcium homeostasis

Martin Zmuda,[1] Eliska Sedlackova,[1] Barbora Pravdova,[1] Monika Cizkova,[2] Marketa Dalecka,[3,4] Ondrej Cerny,[1] Tania Romero Allsop,[1] Tomas Grousl,[5] Ivana Malcova,[1] Jana Kamanova[1]

AUTHOR AFFILIATIONS See affiliation list on p. 18.

ABSTRACT *Bordetella pertussis* is the causative agent of whooping cough in humans, a disease that has recently experienced a resurgence. In contrast, *Bordetella bronchiseptica* infects the respiratory tract of various mammalian species, causing a range of symptoms from asymptomatic chronic carriage to acute illness. Both pathogens utilize type III secretion system (T3SS) to deliver the effector protein BteA into host cells. Once injected, BteA triggers a cascade of events leading to caspase 1-independent necrosis through a mechanism that remains incompletely understood. We demonstrate that BteA-induced cell death is characterized by the fragmentation of the cellular endoplasmic reticulum and mitochondria, the formation of necrotic balloon-like protrusions, and plasma membrane permeabilization. Importantly, genome-wide CRISPR-Cas9 screen targeting 19,050 genes failed to identify any host factors required for BteA cytotoxicity, suggesting that BteA does not require a single nonessential host factor for its cytotoxicity. We further reveal that BteA triggers a rapid and sustained influx of calcium ions, which is associated with organelle fragmentation and plasma membrane permeabilization. The sustained elevation of cytosolic Ca^{2+} levels results in mitochondrial calcium overload, mitochondrial swelling, cristolysis, and loss of mitochondrial membrane potential. Inhibition of calcium channels with 2-APB delays both the Ca^{2+} influx and BteA-induced cell death. Our findings indicate that BteA exploits essential host processes and/or redundant pathways to disrupt calcium homeostasis and mitochondrial function, ultimately leading to host cell death.

IMPORTANCE The respiratory pathogens *Bordetella pertussis* and *Bordetella bronchiseptica* exhibit cytotoxicity toward a variety of mammalian cells, which depends on the type III secretion effector BteA. Moreover, the increased virulence of *B. bronchiseptica* is associated with enhanced expression of T3SS and BteA. However, the molecular mechanism underlying BteA cytotoxicity is elusive. In this study, we performed a CRISPR-Cas9 screen, revealing that BteA-induced cell death depends on essential or redundant host processes. Additionally, we demonstrate that BteA disrupts calcium homeostasis, which leads to mitochondrial dysfunction and cell death. These findings contribute to closing the gap in our understanding of the signaling cascades targeted by BteA.

KEYWORDS *Bordetella*, type III secretion system (T3SS), effector protein BteA, calcium homeostasis, host cell death mechanism

Bordetella pertussis and *Bordetella bronchiseptica,* known as classical bordetellae, colonize the ciliated epithelium of the respiratory tract of various mammals, inducing a spectrum of respiratory symptoms (1, 2). *B. pertussis*, adapted strictly to humans, is the causative agent of pertussis or whooping cough, which was notorious for its high mortality rates in infants before the introduction of the whole cell pertussis

Editor Jeff F. Miller, UCLA School of Medicine, Los Angeles, California, USA

Address correspondence to Jana Kamanova, kamanova@biomed.cas.cz.

Martin Zmuda and Eliska Sedlackova contributed equally to this article. Author order was determined in order of chronological contribution to the project.

The authors declare no conflict of interest.

See the funding table on p. 18.

Received 15 July 2024
Accepted 24 October 2024
Published 21 November 2024

vaccine (wP). The implementation of the wP vaccine substantially reduced pertussis cases. However, with the switch from wP to the acellular pertussis vaccine (aP), there has been a resurgence of pertussis, particularly in adolescents (3). Factors likely contributing to this resurgence include waning immunity in aP-vaccinated individuals and the failure of aP vaccines to elicit Th1/Th17 responses, which is crucial for preventing *B. pertussis* infection, carriage, and transmission (4–6). In contrast, *B. bronchiseptica* has a broader host range but rarely infects humans. Infections caused by *B. bronchiseptica* can range from asymptomatic chronic respiratory carriage to acute illnesses. In dogs, *B. bronchiseptica* causes kennel cough, which is characterized by tracheobronchitis that can progress to bronchopneumonia, especially in puppies (7, 8). In pigs, the bacterium has been associated with atrophic rhinitis, tracheitis, bronchitis, and pneumonia (1, 2, 9).

Cell death is a critical component of host defense against infection, as it eliminates infected cells and triggers immune responses. However, bacterial pathogens have developed sophisticated mechanisms to exploit cell death for their own benefit, facilitating immune evasion and/or nutrient acquisition. The occurrence and manner of cell death are influenced by various factors such as the stage of infection, intensity, host cell type, and physiological state (10, 11). Numerous virulence factors of *B. pertussis* and *B. bronchiseptica* have been identified as inducers of cellular cytotoxicity in a variety of host cells and contribute significantly to the pathogenicity of these bacteria (12–16). One such virulence factor is the type III secretion system (T3SS), which enables the delivery of the cytotoxic effector protein BteA directly from bacterial cytosol into host cells (17, 18). The activity of the T3SS in *B. bronchiseptica* is crucial for persistent colonization of the lower respiratory tract in rats, mice, and pigs, presumably mediated by the actions of the BteA effector (19–21). In addition, increased expression of T3SS genes was associated with the enhanced virulence of the complex I *B. bronchiseptica* 1289 strain isolated from a diseased host compared with the RB50 strain isolated from an asymptomatic host (22, 23). Furthermore, the BteA effector mediates the hypervirulence of complex IV *B. bronchiseptica* isolates (24). Interestingly, the cytotoxicity of BteA of *B. pertussis* is attenuated compared with the considerable BteA-mediated cytotoxicity of *B. bronchiseptica* due to the insertion of an additional alanine at position 503, which may represent an evolutionary adaptation of *B. pertussis* (25). Nevertheless, the role of BteA and T3SS activity in the pathophysiology of pertussis in humans is not yet fully understood.

The 69 kDa effector protein BteA of *B. pertussis* and *B. bronchiseptica* has a modular architecture, consisting of two functional domains: an N-terminal localization/lipid raft targeting (LRT) domain of approximately 130 amino acid residues and a cytotoxic C-terminal domain of approximately 526 and 528 amino acid residues, respectively (26). The N-terminal LRT domain binds negatively charged membrane phospholipids and has a tertiary fold reminiscent of the plasma membrane-targeted 4HBM domain found in a variety of bacterial toxins, including clostridial glucosyltransferase toxins and multifunctional-autoprocessing RTX toxins (MARTX) (26–29). In contrast, the C-terminal cytotoxic domain lacks structural homologs and is solely responsible for cytotoxicity. Indeed, ectopically expressed BteA remains cytotoxic even upon deletion of the LRT domain or the removal of the first 200 N-terminal amino acids (26, 30). The cell death induced by BteA is characterized by its rapid onset, non-apoptotic nature, and independence from caspase-1 (16), although the underlying processes and mechanisms of BteA action are unknown. In this work, we demonstrate that BteA induces host cell death by disrupting calcium homeostasis while exploiting essential processes and/or redundant signaling pathways for its necrotic effects.

RESULTS

BteA-induced cell death is characterized by rapid fragmentation of the endoplasmatic reticulum and mitochondrial networks

To elucidate the mechanisms underlying BteA-induced host cell death, we first examined the morphological changes in epithelial HeLa cells during infection with *B. bronchiseptica* RB50 strain at multiplicity of infection (MOI) of 10:1. Using time-lapse imaging,

we monitored the changes in HeLa cells upon contact with wild-type *B. bronchiseptica* (*Bb*WT) expressing the fluorescent protein mNeonGreen. Shortly after contact, we observed granulation in the cytoplasm of HeLa cells, followed by the formation of plasma membrane blebs, as depicted in Fig. 1A. These blebs continued to expand without retracting, reaching diameters of tens of micrometers. At the same time, we observed shrinkage of the nucleus and its staining with propidium iodide, indicating early damage to the plasma membrane (Fig. 1A; Video S1). In contrast, HeLa cells infected with a *B. bronchiseptica* derivative lacking the *bteA* gene (*Bb*Δ*bteA*) and expressing mNeonGreen at the same MOI exhibited no such morphological changes (Fig. 1A; Video S1).

We confirmed these observations by following the kinetics of plasma membrane permeabilization using the fluorescent DNA binding dye CellTox Green. Infection of HeLa cells with *Bb*WT bacteria at MOI of 50:1 resulted in disruption of cytoplasmic membrane integrity, whereas the *Bb*Δ*bteA* mutant strain failed to induce membrane permeabilization, showing that the observed cytotoxicity of the RB50 strain against HeLa cells was due to the action of the BteA effector (Fig. 1B). As previously reported and also shown in Fig. 1B, we could delay BteA-induced membrane permeabilization by glycine, a plasma membrane-stabilizing amino acid that blocks the opening of non-specific anion channels that lead to colloid osmotic swelling and plasma membrane failure (16). Wild-type *B. pertussis* B1917 (*Bp*WT) at MOI of 50:1 also induced BteA-dependent plasma membrane permeabilization of HeLa cells, but this occurred 6 h post-infection compared with 2 h with *Bb*WT (Fig. 1C). Moreover, increasing the *Bp*WT MOI to 100:1 accelerated this onset by only 2 h. Importantly, as previously demonstrated (25), removing A503 from the BteA effector of *B. pertussis* B1917 (*Bp*ΔA503) resulted in a loss of plasma membrane integrity comparable with that of *Bb*WT (Fig. 1C). These results confirmed the activity of T3SS in *B. pertussis* and the critical role of A503 in BteA cytotoxicity.

To corroborate the processes occurring in HeLa cells just before the BteA-induced plasma membrane blebbing and permeabilization, we used plasmid-encoded fluorescent markers targeted to the endoplasmic reticulum (ER) and mitochondria, specifically export&KDEL-mScarlet and 4xmts-mNeonGreen (31). HeLa cells were transiently transfected with these markers and infected with either *Bb*WT and *Bp*WT strains or their derivatives at MOI 50:1. Cells were fixed at 1 h or 5 h post-infection for fluorescence microscopy analysis. As shown in Fig. 1D, significant fragmentation and vesiculation of the ER and mitochondrial networks was observed in *Bb*WT-infected cells compared with those infected with *Bb*Δ*bteA* derivative or uninfected cells as early as 1 h post-infection. Within 1 h of infection, *Bp*ΔA503 induced similar fragmentation of the ER and mitochondria as *Bb*WT, whereas no significant fragmentation was detected in Hela cells infected by *Bp*WT (Fig. S1A). However, the fragmentation induced by *Bp*WT compared with controls became significant 5 h post-infection, just before plasma membrane permeabilization and cell death, as further shown in Fig. S1B.

In summary, our data demonstrate that BteA from both *B. bronchiseptica* and *B. pertussis* induces fragmentation of ER and mitochondrial networks, which precedes colloid osmotic lysis of HeLa cells. The induction of ER and mitochondrial fragmentation and cell death occurred faster during infection with *B. bronchiseptica* due to the absence of A503 in the BteA effector.

BteA targets essential components of the host cell or genes with redundant functions

To identify host factors essential for BteA-induced cytotoxicity and potentially elucidate the signaling cascades responsible for the observed fragmentation of ER and mitochondria, we next performed a CRISPR-Cas9 forward genetic screen (32–34). This screen employed human embryonic kidney HEK cells, which are similarly sensitive to BteA action as HeLa cells (Fig. S2A) but are more suitable for this approach. To generate HEK-Cas9 mutant library, we used the commercially available GeCKO v2 library (35), divided into sublibraries A and B, each targeting approximately 19,000 human genes with three

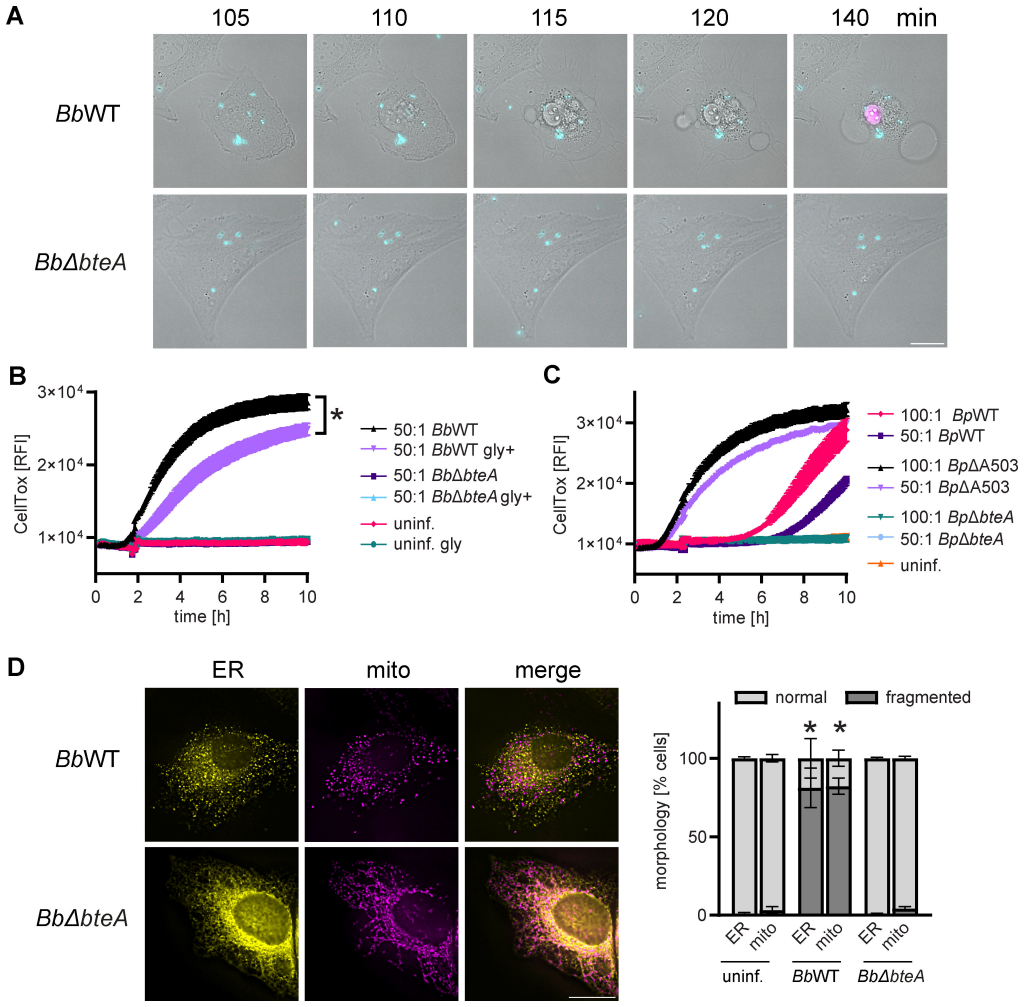

FIG 1 BteA-induced cell death is characterized by fragmentation of the endoplasmatic reticulum and mitochondrial networks. (A) Time lapse analysis of morphological changes and plasma membrane permeabilization in Hela cells. Hela cells were infected with *B. bronchiseptica* wild-type (*Bb*WT) and *BbΔbteA* mutant (*BbΔbteA*), expressing the fluorescent protein mNeonGreen, at MOI of 10:1 in the presence of propidium iodide (5 µg/mL). A sequence of time lapse images is shown. Bright field, gray; bacteria, cyan; propidium iodide, magenta. Scale bar, 20 µm. Data are representative of three independent experiments. (B and C) Comparison of *B. bronchiseptica* and *B. pertussis* cytotoxicity against HeLa cells. HeLa cells were infected with *B. bronchiseptica* (B) or *B. pertussis* (C) wild-type strains and their mutant derivatives at the indicated MOI. Plasma membrane permeabilization was determined using the fluorescent DNA binding dye CellTox Green. For *B. bronchiseptica*, infections were conducted both in the presence (gly+) and absence of glycine (5 mM). Asterisks indicate a statistically significant difference ($P < 0.05$, unpaired two-tailed *t*-test) between *Bb*WT and *Bb*WT gly+ infection samples at 4 h. Data represent the mean ± SEM of a representative experiment out of 2 performed in technical triplicate. (D) Visualization of cellular structures. Hela cells were transfected to express fluorescent proteins tagged with localization signals for endoplasmatic reticulum (ER) and mitochondria (mito). One hour after infection with *Bb*WT and *BbΔbteA* mutant at MOI 50:1, cells were fixed and analyzed by fluorescence imaging. ER, yellow; mitrochondria, magenta. Scale bar, 20 µm. The shown micrographs are representative of two independent experiments from which the organelle morphology was scored. Analysis was performed on at least 100 cells per experiment and condition and is plotted as morphology % ± SEM. Asterisks indicate statistically significant differences ($P < 0.05$, unpaired two-tailed *t*-test) between the % of fragmented ER or mito compared with uninfected cells.

distinct sgRNAs. We packaged these sgRNAs into lentiviral particles and introduced them into Cas9-expressing HEK (HEK-Cas9) cells with MOI of 0.3 to ensure the delivery of a single sgRNA per cell, as depicted in Fig. 2A. Subsequent sequencing of generated HEK-Cas9 sublibraries A and B showed a compact sgRNA distribution, containing the vast

majority of sgRNAs in hundreds of hits to the 15 million normalized reads (Fig. S2B and C). When comparing the number of targeted genes in the respective sublibraries to the theoretically present number of targeted genes, we found that 54 genes in sublibrary A and 53 genes in sublibrary B were not targeted (Fig. S2B and C). However, due to overlap in targeted genes, only 10 genes were not targeted in the combined sublibraries A and B, as shown Fig. 2B. These genes, listed in Table S1, include the phospholamban gene, eight miRNAs, and one non-targeting control guide. Furthermore, as shown in the comparison between Fig. 2B and Fig. S2D, if a gRNA was not detected, it typically constituted one of the six gRNAs present in the theoretical pool. Overall, our analysis of the resulting HEK-Cas9 sublibraries A and B confirmed the successful introduction of sgRNAs of GeCKO v2 library and the preservation of library complexity.

Subsequently, the HEK-Cas9 cell pools were exposed to *Bb*WT at MOI 100:1 for 5 h before *Bb*WT was eliminated by gentamicin. These conditions were previously determined in pilot experiments and induced death in 95% of infected cells. The surviving cells were expanded, and the process was repeated for five rounds of infection to enrich for resistant cells, as depicted in Fig. 2C. Our hypothesis was that infection of transduced cells with *Bb*WT would enrich for sgRNA-directed mutations, which lead to resistance against BteA action due to inactivation of genes required for cell death. However, when comparing the cell pools that survived five rounds of *Bb*WT infection with the parental HEK-Cas9 cells (Fig. 2D), no acquired resistance was detected. Thus, our CRISPR-Cas9 knockout screen failed to identify host genes essential for BteA function.

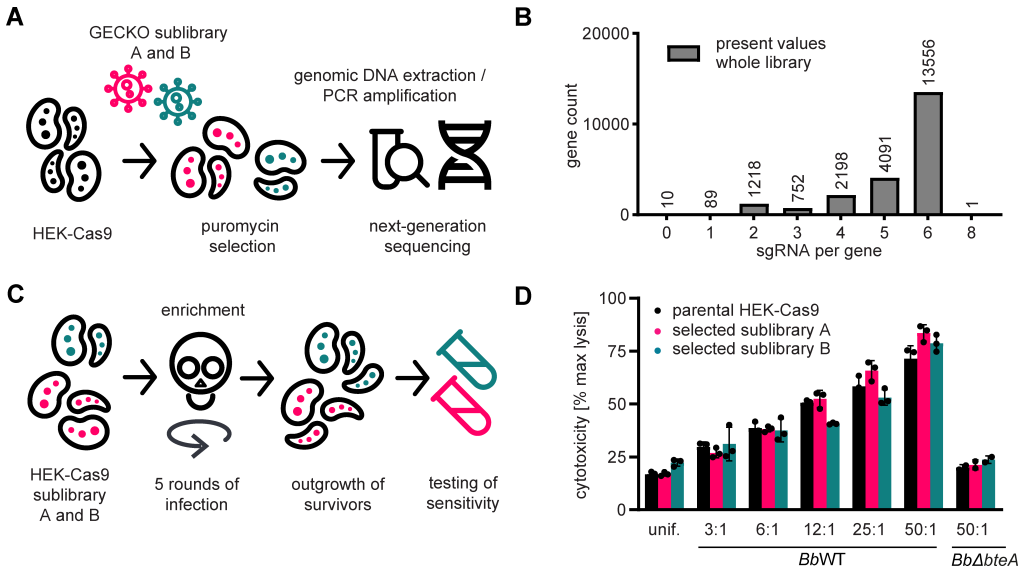

FIG 2 BteA targets essential components of the host cell or genes with redundant functions. (A) Workflow for generating the HEK-Cas9 sublibraries A and B. Sublibraries A and B of the GeCKO v2 library were individually packaged into lentiviral particles and introduced into Cas9-expressing HEK cells. After selection with puromycin and expansion of both cell pools, genomic DNA was extracted, sgRNA was amplified and barcoded, and library complexity was verified by next-generation sequencing. (B) Verification of library complexity in the HEK-Cas9 sublibraries A and B. The number of targeted genes per detected sgRNA count is indicated. (C) Workflow for the enrichment of BteA-resistant cells. HEK-Cas9 sublibraries A and B were subjected to five rounds of selection with *Bb*WT at MOI 100:1 for 5 h per round. Each selection resulted in the death of 95% of infected cells. To stop the infection, the medium containing *Bb*WT was discarded and replaced with a fresh medium containing 100 µg/mL of gentamicin. In between selection rounds, the surviving HEK-Cas9 sublibraries A and B were expanded. (D) Susceptibility of selected HEK-Cas9 sublibraries A and B. Selected HEK-Cas9 sublibraries A and B, and parental HEK-Cas9 cells were infected with *Bb*WT at the indicated MOI. The cytotoxicity was determined as lactate dehydrogenase (LDH) release 6 h post-infection. Susceptibility of selected HEK-Cas9 sublibraries A and B is not significantly different ($P > 0.05$, unpaired two-tailed *t*-test) compared with parental HEK-Cas9 using the corresponding MOI. Data represent the mean ± SEM of a representative experiment out of 2 performed in technical triplicate.

Possible explanations include the redundancy of signaling pathways and the lack of non-essential targets.

BteA disrupts cytosolic calcium homeostasis, leading to permeabilization of cell plasma membrane

Given that the CRISPR-Cas9 screen did not provide mechanistic insights and previous research has shown that changes in the structure of the ER and mitochondria are linked to increased cytosolic calcium levels (36, 37), we investigated whether BteA disrupts cellular calcium homeostasis. To this end, HeLa cells were loaded with the single-wavelength fluorescent Ca^{2+} indicator, Fluo-4/AM (38), and subjected to fluorescence-intensity measurement at 516 nm after infection with *B. bronchiseptica*. As shown in Fig. 3A, *Bb*WT induced cytosolic Ca^{2+} influx, with the intensity and onset of this influx varying based on the used MOI. At MOIs of 50:1 and 25:1, the Ca^{2+} influx peaked around 1 h post-infection, which was followed by a decrease in signal, whereas at MOI of 5:1, the peak of Ca^{2+} influx occurred approximately 2 h after infection. At each MOI, the peak of Ca^{2+} influx induced by *Bb*WT infection preceded the permeabilization of the HeLa cell plasma membrane, as shown by the binding of the DNA dye CellTox Green (Fig. 3B). Importantly, no such Ca^{2+} influx was observed when HeLa cells were infected with the *Bb*Δ*bteA* derivative at the same MOIs, confirming the essential role of BteA in this process.

Subsequently, the response of individual cells to infection with *Bb* strains expressing mScarlet (mSc) at MOI 10:1 was visualized through time-lapse imaging of Fluo-4/AM-loaded HeLa cells. As shown in Fig. 3C and Video S2, the attachment of *Bb*WT to the HeLa cell surface triggered a sustained increase in cytosolic Ca^{2+} levels, which was detected as an increase in Fluo-4/AM fluorescence intensity as early as 30 min after contact. This was followed by BteA-induced plasma membrane blebbing, permeabilization, and cell death. The loss of membrane integrity was noticeable as a decrease in Fluo-4/AM fluorescence intensity. Indeed, inhibition of plasma membrane permeabilization by glycine did not affect the onset of Ca^{2+} influx but prolonged the duration of the Fluo-4/AM signal, as shown in Fig. S3A and B. In a subset of cells, *Bb*WT infection induced cytosolic Ca^{2+} oscillations, as shown in Video S3, which did not immediately lead to the plasma membrane blebbing being strictly associated with a sustained increase in cytosolic calcium levels. Importantly, no major changes in cytosolic Ca^{2+} were observed after infection with *Bb*Δ*bteA* at the same MOI (Fig. 3C; Videos S2 and S3).

To determine the contribution of disrupted cellular calcium homeostasis to BteA-induced cell death, we next analyzed whether the commonly used and rather unspecific calcium channel modulator, 2-aminoethyl diphenylborinate (2-APB), could block BteA-induced cytosolic Ca^{2+} influx and cell death. Importantly, pretreatment with 100 µM 2-APB for 30 min significantly delayed the cytosolic Ca^{2+} influx mediated by BteA, as shown in Fig. 3D. This delay was accompanied by a postponement of BteA-induced membrane permeabilization (Fig. 3E), showing the critical role of cytosolic Ca^{2+} increase in this process.

Overall, our data demonstrate that BteA induces sustained cytosolic Ca^{2+} influx, which triggers cytoplasmic plasma membrane blebbing and permeabilization, ultimately leading to host cell death.

BteA-induced calcium influx is associated with ER and mitochondria fragmentation and yields a pronounced elevation of mitochondrial calcium levels

To gain insight into BteA-induced Ca^{2+} fluxes, we next utilized cytosolic Fluo-4/AM calcium indicator in combination with plasmids encoding red fluorescent Ca^{2+} sensors targeted either to ER or mitochondria, ER-LAR-Geco, and mito-LAR-Geco (39), respectively.

First, HeLa cells were transiently transfected with ER-LAR-Geco, loaded with Fluo-4/AM, and subjected to infection with *BbWT*. The increase in cytosolic Ca^{2+} concentration correlated with fragmentation of the ER network, as shown in Fig. 4A and Video S4. Quantification of changes in ER-LAR-Geco relative fluorescence intensity (RFI)

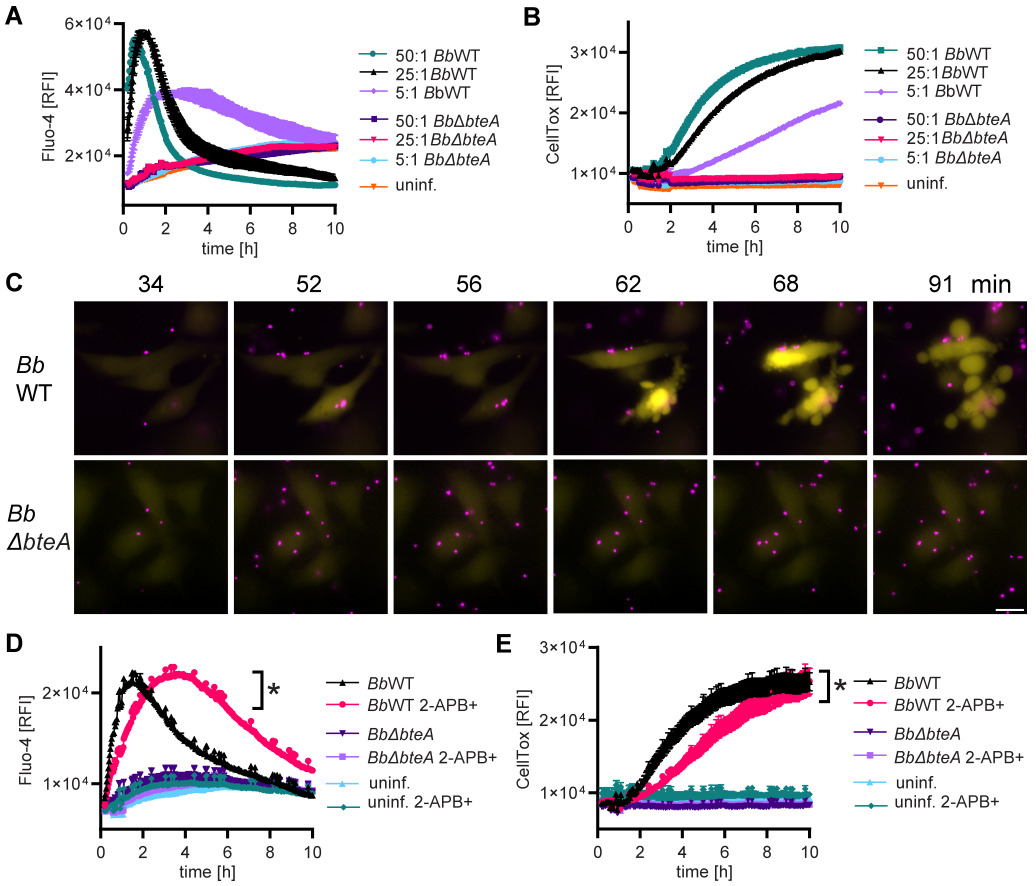

FIG 3 BteA disrupts cytosolic calcium homeostasis, leading to the permeabilization of cell plasma membrane. (A and B) Calcium influx precedes *B. bronchiseptica*-induced plasma membrane permeabilization. HeLa cells were infected with *Bb*WT and *BbΔbteA* mutant at the indicated MOI. Calcium influx was monitored using cytosolic Ca^{2+} indicator Fluo-4/AM (A), whereas plasma membrane permeabilization was determined in parallel wells by fluorescent DNA binding dye CellTox Green (B). Data represent the mean ± SEM of a representative experiment out of 3 performed in technical duplicate. (C) Calcium imaging. HeLa cells loaded with cytosolic Ca^{2+} indicator Fluo-4/AM were infected with *Bb*WT and *BbΔbteA*, expressing the fluorescent protein mScarlet (mSc), at MOI of 10:1. Sequence of time lapse images is shown. Bacteria, magenta; cytosolic Ca^{2+} indicator Fluo-4/AM, yellow. Scale bar, 20 µm. Data are representative of two independent experiments. (D and E) Treatment with 2-APB delays calcium influx and host cell death. HeLa cells were pre-incubated with 100 µM 2-APB (2-APB+) for 30 min, or left untreated, before being infected with *Bb*WT or *BbΔbteA* derivative at MOI 25:1. Calcium influx was assessed using Fluo-4/AM Ca^{2+} indicator, (D) whereas plasma membrane permeabilization was determined in parallel wells by fluorescent DNA binding dye CellTox Green (E). Asterisks indicate a statistically significant difference ($P < 0.05$, unpaired two-tailed *t*-test) between *Bb*WT and *Bb*WT 2-APB+ infection samples at 1 h 30 min (maximum of *Bb*WT Fluo-4/AM signal) (D) and at 4 h (E). Data represent the mean ± SEM of a representative experiment out of three performed in technical duplicate.

(Fig. 4A; Fig. S4) revealed no significant changes before cytosolic Ca^{2+} influx ($P > 0.05$, compared with uninfected cells). However, a modest but statistically significant 6% increase in ER-LAR-Geco RFI was observed during cytosolic Ca^{2+} elevation.

In contrast, cells expressing mito-LAR-Geco (Fig. 4B; Fig. S5) showed a pronounced and statistically significant increase in mitochondrial Ca^{2+} levels at the time of cytosolic Ca^{2+} increase. This increase in mitochondrial Ca^{2+} levels preceded mitochondrial fragmentation and plasma membrane blebbing, as evidenced in Fig. 4B and Video S5. Consistent results were obtained when cell mitochondria were visualized using MitoTracker (Fig. S6; Video S6). Thus, BteA-induced Ca^{2+} influx is associated with the fragmentation of the ER and mitochondria and leads to pronounced elevation of mitochondrial Ca^{2+} levels. We also detected a slight but statistically significant elevation of ER Ca^{2+} levels.

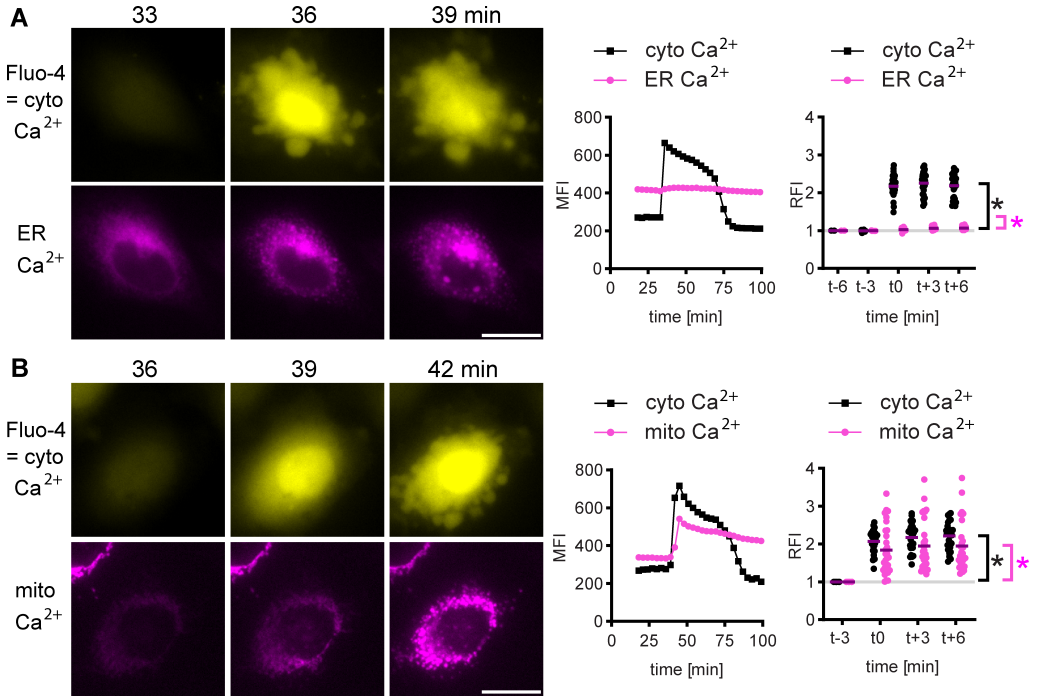

FIG 4 BteA-induced calcium influx correlates with ER and mitochondria fragmentation and yields pronounced elevation of mitochondrial calcium levels. (A) ER calcium imaging. Hela cells, transfected to express ER-targeted red Ca^{2+} sensor ER-LAR-Geco, were loaded with the cytosolic Ca^{2+} indicator Fluo-4/AM and infected with *Bb*WT at MOI of 10:1. A sequence of time-lapse images is shown. Cytosolic Ca^{2+} indicator Fluo-4/AM, yellow; ER Ca^{2+} sensor ER-LAR-Geco, magenta. Scale bar, 20 µm. Data are representative of two independent experiments. The graph in the middle depicts the mean fluorescence intensity of the shown cell quantified over time. The right graph shows the relative fluorescence intensities of individual cells (n = 30) at the time of calcium influx. Asterisks indicate a statistically significant difference (P < 0.05, unpaired two-tailed t-test) between t-3 and t0. Cyto Ca^{2+}, black asterisk; ER Ca^{2+}, magenta asterisk. (B) Mitochondrial calcium imaging. Hela cells, transfected to express mitochondria-targeted red Ca^{2+} sensor mito-LAR-Geco, were loaded with the cytosolic Ca^{2+} indicator Fluo-4/AM, and infected with *Bb*WT at MOI of 10:1. A sequence of time-lapse images is shown. Cytosolic Ca^{2+} indicator Fluo-4/AM, yellow; mitochondrial Ca^{2+} sensor mito-LAR-Geco, magenta. Scale bar, 20 µm. Data are representative of two independent experiments. The graph in the middle depicts the mean fluorescence intensity of the shown cell quantified over time. The right graph shows the relative fluorescence intensities (RFIs) of individual cells (n = 30) at the time of calcium influx. Asterisks indicate a statistically significant difference (P < 0.05, unpaired two-tailed t-test) between t-3 and t0. Cyto Ca^{2+}, black asterisk; mito Ca^{2+}, magenta asterisk.

BteA induces loss of mitochondrial membrane potential that is accompanied by mitochondrial swelling and cristolysis

To test the impact of BteA-induced mitochondrial Ca^{2+} uptake on mitochondrial function, we next evaluated mitochondrial membrane potential using tetramethylrhodamine (TMRM), which accumulates in healthy mitochondria. A loss of mitochondrial membrane potential leads to the disappearance of the TMRM signal. Indeed, mitochondria play a critical role in maintaining Ca^{2+} homeostasis by sequestering calcium ions. However, excessive Ca^{2+} uptake by mitochondria, known as mitochondrial calcium overload, can trigger mitochondrial swelling, the opening of the mitochondrial permeability transition pore (mPTP), and loss of mitochondrial membrane potential, ultimately leading to cell death (40, 41).

As shown in Fig. 5A, Fig. S7, and Video S7, time-lapse imaging revealed that BteA-induced Ca^{2+} influx results in a loss of mitochondrial membrane potential. In addition, electron microscopy showed extensive cytoplasmic vacuolization in *Bb*WT-infected cells (Fig. S8). To examine mitochondrial ultrastructure, we next performed correlative 3D imaging by combining fluorescence microscopy with focused ion beam-scanning

electron microscopy (FIB-SEM). As shown in Fig. 5B and Fig. S9, *Bb*WT-infected cells displayed clear signs of mitochondrial swelling and the loss of mitochondrial cristae. However, neither ruthenium 360, an inhibitor of the mitochondrial calcium uniporter channel, nor cyclosporine A, an inhibitor of mPTP, was able to block BteA-induced plasma membrane permeabilization (Fig. S10). These data indicate that although BteA-induced mitochondrial Ca^{2+} uptake correlates with mitochondrial failure, mitochondrial damage alone is not solely responsible for the execution of BteA-induced cell death. Alternatively, it is possible that treatments aimed at preventing mitochondrial damage are insufficient to counteract the sustained Ca^{2+} influx caused by BteA. In fact, pre-treatment with ruthenium 360 failed to prevent the loss of mitochondrial membrane potential (Video S8).

DISCUSSION

Our study demonstrates that injection of *Bordetella* type III effector protein BteA into the host cell triggers a cytosolic Ca^{2+} influx that disrupts cellular calcium homeostasis. This sustained increase in cytosolic Ca^{2+} is detectable within minutes of bacterial contact and leads to mitochondrial Ca^{2+} overload, plasma membrane blebbing, and early membrane damage. Furthermore, the CRISPR-Cas9 screen shows that BteA targets critical and/or redundant cellular survival mechanisms and is not dependent on a single non-essential host factor for its cytotoxic effects.

The type III secretion effector BteA of classical *B. bronchiseptica* and *B. pertussis* is a potent cytotoxin that causes cell death in a variety of cells, including epithelial cells and macrophages (16, 17, 19, 42). Previous studies have shown that BteA induces morphological changes in rat epithelial lung L2 cells within just 25 min (42, 43). In our time-lapse experiments, when we centrifuged *B. bronchiseptica* at MOI of 10:1 onto HeLa cells and examined the cells, we detected increased levels of cellular Ca^{2+} already during the initial microscope focusing. No more than 10 min after adding the bacteria to the host cells. Similarly, spectrophotometric measurements of a whole cell population infected with MOI of 25:1 showed elevated levels of Ca^{2+} at the first collected data point. When the bacteria during time-lapse microscopy were added without centrifugation so that we could follow their sedimentation on the cell surface, we observed a sustained increase in cytosolic Ca^{2+} as early as 30 min after bacterial contact with the host cell. The plasma membrane blebbing and permeabilization were observed after another 30–60 min. These results demonstrate the efficiency of T3SS-mediated BteA delivery into the host cell and BteA potency to disrupt cellular signaling and cause cell death.

The most prominent feature of the BteA-induced morphological changes during cell death was the swelling of the cytoplasm and the formation of balloon-like, non-retracting plasma membrane blebs. This observation is consistent with previous studies (16, 30) and is a common manifestation of cell injury associated with a lytic form of cell death. In fact, regulated cell death can be categorized into lytic and non-lytic forms. Lytic forms, such as pyroptosis and necroptosis, involve the formation of pores or breaches in the plasma membrane and the expansion of the cytoplasmic compartment due to an ionic imbalance. This process ultimately leads to cell rupture and the release of intracellular contents into the extracellular space. In contrast, non-lytic forms, such as apoptosis, involve the coordinated disintegration of dying cells into smaller fragments without compromising the integrity of the cytoplasmic membrane (44). Similar to necrosis, apoptosis is also characterized by blebbing of the plasma membrane. In apoptotic blebbing, however, there are repeated protrusions and retractions of the plasma membrane, which lead to the formation of apoptotic bodies. In necrotic blebbing, on the other hand, no retractions take place, allowing blebs to grow larger (45). The signaling processes underlying blebbing are complex. Key events in the formation of blebs include disruption of the actomyosin cell cortex and its interaction with the plasma membrane and regulation of cytoplasmic fluidity. Importantly, Ca^{2+} is an important regulator of actin-binding proteins that control the dynamics of the actin cytoskeleton and are involved in the regulation of bleb formation (46, 47). An increase in Ca^{2+}

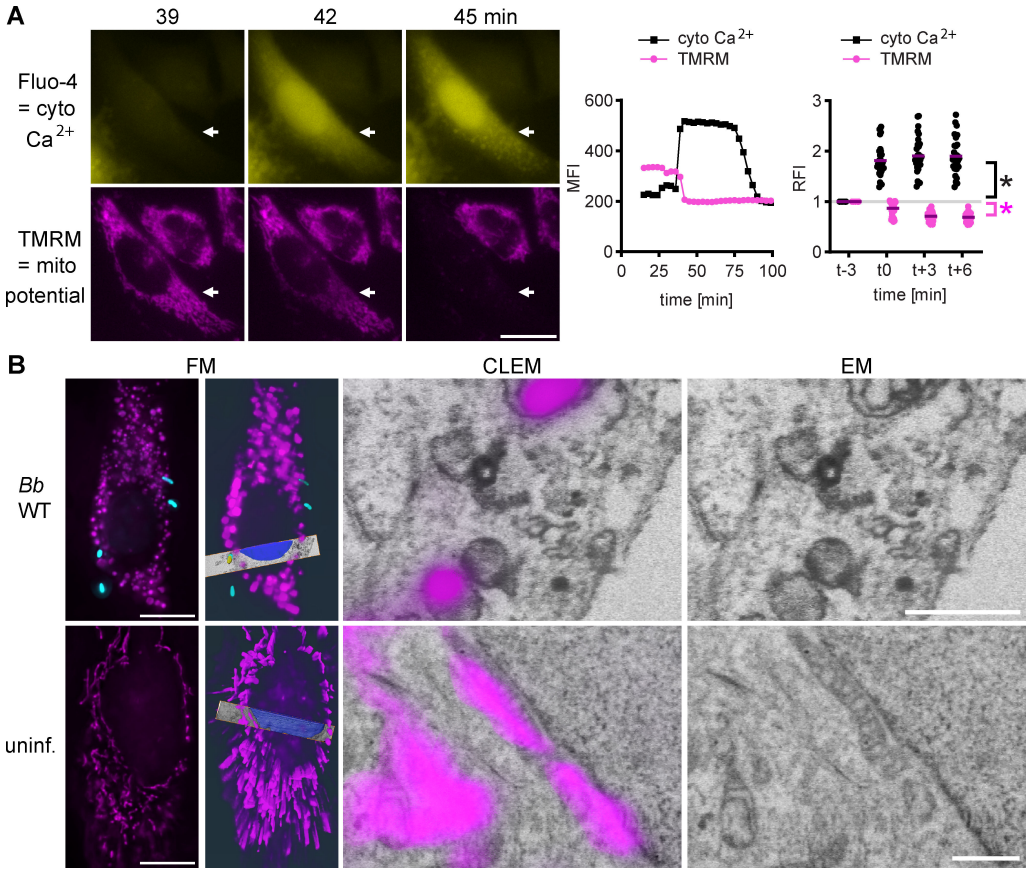

FIG 5 BteA induces loss of mitochondrial membrane potential, mitochondrial swelling, and cristolysis. (A) BteA-induced calcium influx precedes loss of mitochondrial membrane potential. HeLa cells were loaded with the mitochondrial membrane potential indicator TMRM and the cytosolic Ca^{2+} indicator Fluo-4/AM, which was followed by infection with *Bb*WT at MOI 10:1. Sequence of time lapse images is shown. Cytosolic Ca^{2+} indicator Fluo-4/AM, yellow; TMRM, magenta. Scale bar, 20 µm. Data are representative of two independent experiments. The graph in the middle depicts the mean fluorescence intensity of the shown cell (white arrow) quantified over time. The right graph shows the relative fluorescence intensities of individual cells (n = 30) at the time of calcium influx. Asterisks indicate statistically significant difference (P < 0.05, unpaired two-tailed t-test) between t-3 and t-0. Cyto Ca^{2+}, black asterisk; TMRM, magenta asterisk. (B) Correlative light and electron microscopy of mitochondria in HeLa cells. HeLa cells, transfected to express mitochondria-targeted monomeric hyperfolder YFP fluorescent protein, were either infected with mScarlet-expressing *Bb*WT at MOI 10:1 for 0.5 h or left untreated. Fluorescence imaging was performed during the fixation period to capture bacteria and mitochondrial structures. Samples were then prepared for electron microscopy and FIB-SEM imaging. Data visualization was processed in Amira 3D 2024.1 software. Mitochondria, magenta; bacteria, cyan. Scale bar FM, 10 µm; scale bar EM, 1 µm.

leads to the fragmentation of F-actin through the activation of gelsolin and inverted formin-2 (INF2) (48, 49) and also increases cytoplasmic fluidity in the expanding bleb (50). In addition, Ca^{2+} activates calpains, cytoplasmic cysteine proteases of the papain family, which cleave various substrates, including cytoskeletal proteins such as spectrin, E-cadherin, and vinculin, thus contributing to cell damage (51, 52).

It is important to point out that a sustained increase in cytosolic Ca^{2+} is an upstream event in BteA-induced cytotoxicity, as summarized in Fig. 6. First, this increase in cytosolic Ca^{2+} happens quickly and precedes any nonspecific damage to the plasma membrane. Second, inhibition of plasma membrane permeabilization with glycine, which blocks the opening of nonspecific anion channels, has no effect on the onset of Ca^{2+} influx. Finally, the calcium channel modulator 2-APB delays both Ca^{2+} influx and plasma membrane permeabilization. Interestingly, time-lapse experiments with fluorescence images taken every 3 min also showed that infection with *Bb*WT, in contrast to infection with the

mutant *Bb*Δ*bteA* strain, induces cytoplasmic Ca^{2+} oscillations in a subset of HeLa cells. These oscillations occurred both in the cells prior to the sustained Ca^{2+} increase and in the cells that did not show a sustained Ca^{2+} increase during the imaging period. We hypothesize that these oscillations may be a coping mechanism of the cells in response to BteA action. Alternatively, it could be a response to ATP release from neighboring lysed cells, which has been described as a trigger for Ca^{2+} oscillations (53). The relationship of these oscillations to BteA-induced cell death remains to be investigated.

The 69 kDa BteA effector comprises two different functional domains. The N-terminal region, consisting of 130 amino acids, binds to negatively charged membrane phospholipids and localizes BteA to the plasma membrane (26, 28, 29), and the C-terminal region, consisting of 526 amino acids in *B. pertussis* and 528 amino acids in *B. bronchiseptica*, which is solely responsible for cytotoxicity (25, 26). No known homologs exist for the C-terminal region, and prediction and homology search tools have been unable to elucidate the mechanism underlying its cytotoxicity (18). Even models generated by the AlphaFold prediction server (54) exhibit low confidence in the structural prediction of this region. The kinetics of cell death induced by *Bb*WT and *Bp*WT strains can be linked to the presence or absence of alanine 503 in the BteA effector, although it is unclear how this insertion affects the BteA structure (25). Analyses using transmembrane predictors such as DeepTMHMM (55), https://dtu.biolib.com/DeepTMHMM, indicate no transmembrane alpha-helical or beta-barrel segments within the BteA molecule, suggesting it does not form membrane pores. Consequently, the potency and rapid effect of BteA on disrupting calcium ion homeostasis suggest that BteA either affects host cell enzymes and/or membrane channels or possesses enzymatic activity itself.

The delivery of BteA into the host cell cytosol is required for cytotoxicity. Mutant strains of *B. bronchiseptica* lacking translocon components such as BopB, BopD, and Bsp22, which are required for the translocation of BteA into the host cells (but not for its secretion into the cell medium), do not induce cell death (43, 56–58). In contrast, heterologous expression of BteA causes cytotoxicity in both mammalian cells and *S. cerevisiae* (25, 26), which indicates that the pathways activated by BteA that lead to cytotoxicity are conserved across species. Our CRISPR-Cas9 forward genetic screen, which applied stringent selective pressure, further suggests that the host cell factors targeted by BteA are essential and/or that the mechanism of BteA action is redundant. This screen aimed to identify genes that are required for the cytotoxicity of BteA by inactivating them using the GeCKO v2 library (35). Despite the successful introduction of the sgRNA library, targeting approximately 19,000 genes and missing only 10 (see Table S1) into HEK-Cas9 cells, we were unable to select resistant cells and pinpoint specific host genes essential for BteA-induced cell death. More refined or complementary genetic screens might be necessary to identify host factors, which contribute redundantly

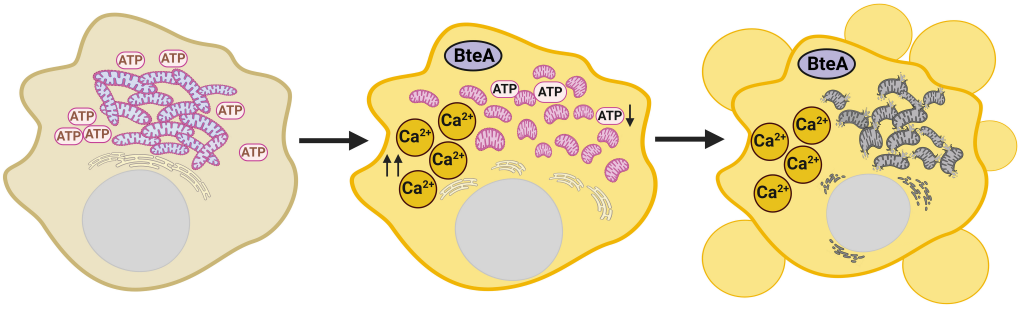

FIG 6 The schematic model of BteA-induced cell death. Upon delivery, BteA rapidly triggers a sustained elevation of cytosolic Ca^{2+} levels, which leads to mitochondrial Ca^{2+} overload. This disrupts mitochondrial membrane potential, causing swelling and cristae loss. The resulting mitochondrial dysfunction may activate the mitochondrial permeability transition pore (mPTP), driving plasma membrane blebbing and early cell damage. Inhibition of Ca^{2+} influx with the calcium channel modulator 2-APB delays these effects, underscoring the critical role of calcium dysregulation in BteA-induced cell death. Created in BioRender [Kamanova, J. (2024) BioRender.com/l36y378].

and/or partially. These screens should use lower selective pressure to better differentiate between cells with and without the target gene knockouts, although this approach also presents challenges. The amount of BteA delivered by bacteria is not precisely controlled, resulting in variable delivery among cells, and using a stable cell line with inducible BteA expression is also not straightforward. We have been unsuccessful in constructing a stable HEK-Cas9 cell line expressing doxycycline-inducible *Bb*BteA due to promoter leakiness. Additionally, although we managed to construct a HEK-Cas9 line with inducible expression of the less toxic *Bp*BteA, this cell line was unstable, leading to the loss of the *BpbteA* gene after several passages. An interesting alternative to explore is gain-of-function genomic screens, including CRISPR-based gene activation screens (59), which may help uncover potential targets and mechanisms that may have been missed in the current study.

The lack of identified genes required for BteA cytotoxicity aligns well with the observations that BteA rapidly disrupts calcium homeostasis, which is a crucial cellular signaling mechanism. Indeed, calcium ions serve as a universal cellular messenger but can also become toxic and cause cell death. In a resting cell, the cytoplasmic Ca^{2+} concentration is relatively low, about 100 nM, similar to that in the mitochondria. In contrast, the Ca^{2+} concentration in the ER is between 100 µM and 1 mM, making the ER the main calcium ion reservoir in the cell and a crucial player in coordination with other organelles and the plasma membrane (60, 61). During cell stimulation, the cytosolic Ca^{2+} concentration increases approximately 10 times to 1 µM due to the release of Ca^{2+} from the ER or the influx of extracellular Ca^{2+}. In addition, the ER transmits Ca^{2+} signals to the mitochondria via transport systems located at the mitochondria-associated ER membranes (MAMs) and relying on the IP3 receptors (IP3R) and the mitochondrial calcium uniporter (MCU) (62, 63). To gain insight into the disruption of calcium homeostasis by the action of BteA, we monitored cellular Ca^{2+} fluxes triggered by BteA. Although we observed oscillatory cytosolic Ca^{2+} increases, indicating Ca^{2+} release from the ER via IP3R, we did not detect any release of Ca^{2+} from ER, which would precede sustained cytosolic Ca^{2+} elevation. This could be due to two reasons. First, the low-affinity intensiometric red fluorescent Ca^{2+} sensor ER-LAR-Geco might lack the sensitivity to detect changes in ER Ca^{2+} concentration. Second, the 3-min intervals used to acquire the fluorescence images may have allowed any decrease in ER Ca^{2+} concentration to reverse. Depletion of ER Ca^{2+} stores triggers an influx of Ca^{2+} from the extracellular space, known as capacitative Ca^{2+} influx or store-operated Ca^{2+} entry (SOCE), which increases cytosolic calcium levels and replenishes the ER (60). In fact, at the time of the cytosolic Ca^{2+} increase, we detected a slight but statistically significant increase in ER Ca^{2+} levels. Future studies should investigate how BteA triggers Ca^{2+} influx and which cellular components are involved. Although the calcium channel modulator 2-APB is useful in assessing the general importance of cellular calcium levels, it is not suitable for detailed mechanistic experiments. 2-APB was initially discovered as an inhibitor of the IP3R in the ER but was later also shown to modulate SOCE and block plasma membrane TRPC and TRPM channels (64–67).

Importantly, unlike changes in the ER Ca^{2+} levels, we demonstrate that BteA causes a sustained Ca^{2+} influx into the mitochondria. This influx is crucial as mitochondrial Ca^{2+} dynamics play a critical role in determining cellular outcomes. Rhythmic low-level Ca^{2+} oscillations enhance mitochondrial ATP production, whereas insufficient Ca^{2+} uptake slows cell proliferation. Furthermore, prolonged Ca^{2+} accumulation can trigger cell death (62). Mitochondria can accumulate 10–20 times more Ca^{2+} than the cytosolic compartment; however, excessive Ca^{2+} accumulation can trigger the opening of the mitochondrial permeability transition pore (mPTP) either directly or indirectly (62, 68, 69). This process disrupts mitochondrial functions, including ATP synthesis and mitochondrial membrane potential, ultimately leading to mitochondrial rupture and release of apoptogenic factors such as cytochrome c. In scenarios, where the cell lacks glycolytic ATP sources, this cascade results in mPT-driven necrotic cell death. In contrast, with sufficient ATP levels, early membrane damage is blocked, and apoptogenic factor

release initiates ATP-dependent caspase activation and apoptosis (70, 71). We show that BteA-triggered elevation of cytosolic Ca^{2+} precedes loss of mitochondrial membrane potential and early membrane permeabilization (Fig. 6). Transmission electron microscopy additionally confirms mitochondrial swelling and cristolysis. These results demonstrate that BteA induces mitochondrial dysfunction, consistent with the concept of mitochondrial Ca^{2+} overload and mPTP-mediated necrosis.

Limitations of the study

Although our study provides substantial insights into the cytotoxicity of the *Bordetella* type III effector protein BteA, the experiments were primarily carried out using HeLa and HEK cells. Although these cell lines are valuable for mechanistic studies and analyzing the disruption of cellular signaling by virulence factors, they do not fully replicate the complexity of an *in vivo* environment. This includes the resistance of certain cell types to Ca^{2+} cytotoxicity and their capacity to maintain ATP levels.

MATERIALS AND METHODS

Bacterial strains and growth conditions

The bacterial strains used in this study are listed in Table S2. *Escherichia coli* strain XL1-Blue was used for plasmid construction, and *E. coli* strain SM10λ pir was used for plasmid transfer into *B. bronchiseptica* RB50 by bacterial conjugation. *E. coli* strains were cultivated at 37°C in Luria-Bertani (LB) agar or LB broth. When appropriate, the LB medium was supplemented with chloramphenicol (30 µg/mL), kanamycin (30 µg/mL), or ampicillin (100 µg/mL) for *E. coli* XL1 Blue and chloramphenicol (15 µg/mL) for *E. coli* SM10λ. *B. bronchiseptica* RB50 and *B. pertussis* B1917 strains were grown on Bordet-Gengou (BG) agar medium (Difco, USA) supplemented with 1% glycerol and 15% defibrinated sheep blood (Lab- MediaServis, Jaromer, Czech Republic) at 37°C and 5% CO_2. Liquid cultures were done in a modified Stainer-Scholte (SSM) medium with reduced L—glutamate (monosodium salt) concentration (11.5 mM, 2.14 g/l) and without $FeSO_4.7H_2O$ to maximize the expression of T3SS, as reported previously (25). Culture medium of *B. bronchiseptic*a RB50 harboring pBBRI plasmid (Table S2) was further supplemented with chloramphenicol (30 µg/mL).

Plasmid construction and introduction into *B. bronchiseptica*

Plasmids used in this study are listed in Table S3 and were constructed using the Gibson assembly strategy (72). The GroES promotor (391 nt, NC_002927.3, 1 041 354–1 041 744) was amplified from chromosomal DNA of *B. bronchiseptica* RB50, whereas the mNeonGreen coding sequence was amplified from 4xmts-mNeonGreen vector (Addgene item # 98876) using Herculase II Phusion DNA polymerase (Agilent, USA). The pBBRI plasmids encoding mScarlet and mNeonGreen fluorescent proteins were introduced into *B. bronchiseptica* cells by conjugation, using *E. coli* SM10 λpir as plasmid donor strain. The *B. bronchiseptica* conjugants were selected on Bordet-Gengou (BG) blood agar plates supplemented with chloramphenicol (60 µg/mL) and cephalexin (10 µg/mL).

Cell culture and transfection

HeLa (ATCC CCL-2, human cervical adenocarcinoma), 293T (ATCC CRL-3216, human epithelial kidney cell line), and HEK-Cas9 (293[HEK-293] Cas9, ATCC CRL-1573Cas9, human embryonic kidney cell line constitutively expressing Cas9 from *Streptococcus pyogenes*) were cultivated in Dulbecco's Modified Eagle Medium (DMEM, Sigma, USA) supplemented with 10% fetal bovine serum (DMEM-10%FBS) at 37°C and 5% CO_2. Transfections of HeLa cells with plasmids encoding fluorescent markers for ER and mitochondria visualization (Table S3), or Ca^{2+} sensors ER-LAR-GECO and mito-LAR-GECO (Table S3), were performed at 50% cell confluency using PEI MAX transfection reagent

(Polysciences). After 24 h, 5×10^4 of transfected cells were seeded per coverslip in 24-well plates, 1×10^5 per well in four-well glass-bottom dishes (Cellvis), or 1×10^5 per gridded glass bottom dish (Mattek) and allowed to adhere overnight before infection.

Time-lapse live cell imaging for the determination of morphological changes and plasma membrane integrity

In total, 1×10^5 HeLa cells were seeded per well in a four-well glass-bottom dish (Cellvis). The next day, *Bb*WT expressing the fluorescent protein mNeonGreen (*Bb*WT/mNG) or its Δ*bteA* mutant (*BbΔbteA*/mNG) (Table S2) were added at MOI 10:1 along with propidium iodide (PI, 5 µg/mL). After centrifugation (5 min, 120 g), a glass-bottom dish was transferred to a prewarmed stage-top incubation chamber of a motorized fluorescence microscope (IX-83, Olympus, Japan) equipped with sCMOS camera Photometrics Prime 95B. Bright-field and fluorescence microscopic images were acquired using a 60× oil immersion objective (PLAPON60XOSC2, NA = 1.4) at a temperature of 37°C and 5% CO_2 during the imaging process. CellSens software was used for adjustment, image acquisition, and recording sequential images in 16-bit mode at 5-min intervals. Fluorescence was captured using quadruple dichroic mirror DAPI/FITC/TRITC/CY5 with filter block exc. 555/25 nm, em. 605/52 nm for PI, and exc. 490/20 nm, em. 525/36 nm for mNG.

Ninety-six-well plate cytotoxicity assay

Cytotoxicity of *B. bronchiseptica* and *B. pertussis* toward HeLa and HEK-Cas9 was determined as changes in cell membrane integrity using the fluorescent DNA binding dye CellTox Green (Promega, Cat. No. G8743), as described previously (29). In brief, 2×10^4 of HeLa or HEK-Cas9 cells per well were seeded in a 96-well black/clear bottom plate (Corning, USA) in DMEM-10%FBS. The next day, *B. bronchiseptica* or *B. pertussis* strains were added at the indicated MOI along with CellTox Green reagent. The plate was centrifuged (5 min, 120 g) and placed inside the chamber with 37°C and 5% CO_2 of the TecanSpark microplate reader (Tecan, Switzerland). Fluorescence measurements at 494ex/516em with a 10 nm bandwidth for both were performed at defined time intervals for 10 h. If appropriate, HeLa cells were pre-treated with 2-aminoethyl diphenylborinate (2-APB) at 100 µM for 30 min, ruthenium 360 at 10 µM, or cyclosporin A at 1 µM for 60 min prior to *B. bronchiseptica* infection. Additionally, glycine at 5 mM was added 5 min before infection when required.

Visualization of cellular organelles in fixed cells

In total, 5×10^4 of HeLa cells transiently expressing fluorescent markers for ER and mitochondria visualization (Table S3) were seeded per coverslip and incubated at 37°C and 5% CO_2. The next day, HeLa cells were infected with the indicated *B. bronchiseptica* or *B. pertussis* strains at a MOI 50:1. Added bacteria were centrifugated (5 min, 120 g) onto the cell surface, and samples were fixed by 4% formaldehyde solution in PBS (20 min, RT) 1 and 5 h post-infection. Coverslips were then rinsed with distilled water and mounted onto microscope glass slides using Vectashield mounting medium (Vector Laboratories, USA). Fluorescence microscopy was performed using a motorized fluorescence microscope (IX-83, Olympus, Japan) equipped with sCMOS camera Photometrics Prime 95B with 100 × oil-immersion objective (UPLXAPO100XOPH, N.A. = 1.45). Fluorescence was captured using quadruple dichroic mirror DAPI/FITC/TRITC/CY5 with filter block exc. 555/25 nm, em. 605/52 nm for mScarlet, and exc. 490/20 nm, em. 525/36 nm for mNG. Images were collected in a 16-bit format using CellSens software, with Z-stacks taken with 0.26 µm z-steps and deconvolution performed with Advanced Maximum Likelihood (AMLE) filters. A single focal plane of a Z-stack is presented in all figures.

Production of lentiviral vector library and genome-wide CRISPR-Cas9 knockout screen in HEK-Cas9 cells

The production of lentiviral vector library GeCKO v2 (Addgene item #1000000049 [35]) consisting of sublibraries A and B and preparation of the corresponding sublibraries of HEK-Cas9 cells were done according to the protocol reported by Joung et al. (73). In brief, 6×10^6 of 293T cells per T75 flask were seeded, with a total of 24 T75 flask utilized. The next day, each T75 flask was co-transfected with 4.5 µg of pCMV-VSV-G, 6.5 µg of psPAX2, and 9 µg of either GeCKO v2 human sublibrary A or B (Table S3) using PEI MAX transfection reagent (Polysciences). After 48 h, the supernatant of the 293T cells containing packaged vector sublibrary A or B was collected, filtered through a 0.45-µm filter, and stored at −80°C. To determine the viral titer in the collected supernatants, HEK-Cas9 cells were transduced in a 96-well white/clear bottom plate (Corning, USA) using varying amounts of the supernatant in the presence of polybrene (8 µg/mL). Following supernatant addition, cells were centrifuged (2 h, 1,000 *g*) and cultivated for 24 h before selection with puromycin (0.6 µg/mL). After 5 days, the number of surviving cells was assessed using Cell Titer Glo (Promega, Cat.no. G7570), and the virus titer was calculated.

Subsequently, HEK-Cas9 sublibraries A and B were prepared through lentivirus spin infection of HEK-Cas9 cells at MOI of 0.3:1 to ensure a single sgRNA delivery per cell, as follows. HEK-Cas9 cells were seeded into 6-well plates, lentivirus was added in the presence of polybrene (8 µg/mL), and plates were centrifugated (2 h, 1,000 *g*). A total of 10^8 HEK-Cas9 cells were transduced per sublibrary to achieve coverage of >500 cells per sgRNA. Twenty-four hours post-transduction, HEK-Cas9 cells were selected with puromycin (0.6 µg/mL) for 5 days. The surviving cells were expanded, and HEK-Cas9 libraries were cryostocked at 10^8 cells per sublibrary stock. The preservation of complexity in the sublibraries was next assessed by next-generation sequencing. In brief, genomic DNA from 10^8 cells per sublibrary was harvested using a Blood & Cell Culture DNA Maxi kit (QIAGEN, Cat. no. 13362), and the sgRNA regions were amplified and barcoded using a PCR reaction, as described in (73). The barcoded PCR products were pooled in equimolar ratios and concentrated using Zymo-Spin V Columns (Zymo Research, Cat.no. C1012-25). The concentrated PCR products were separated on a 2% agarose gel and extracted using the DF300 Gel/PCR DNA Fragments Extraction Kit (Geneaid, Cat.no. DF300). DNA concentration in the samples was determined by Qubit dsDNA HS Assay Kit (Invitrogen), and product length was verified using Agilent High Sensitivity DNA Kit. The samples were sequenced on the Illumina NextSeq 2000 platform (single-end, 100 cycles). Sequence data were analyzed and aligned to the sequence reads in a reference file of all sgRNA sequences in sublibrary A and B, which is provided by Addgene.

For positive selection of prepared GeCKO v2 HEK-Cas9 sublibraries A and B by infection with *B. brochiseptica* RB50 wild type, we employed 10^8 cells per HEK-Cas9 sublibrary (ensuring >1,500 coverage per sgRNA). Each HEK-Cas9 sublibrary was distributed across five 15 cm Petri dishes and infected with *Bb*WT at MOI of 100:1. The infection was allowed to proceed at 37°C and 5% CO_2 for 5 h. To stop the infection, the medium containing *Bb*WT was discarded and replaced with a fresh medium containing gentamicin (100 µg/mL). These conditions resulted in the death of approximately 95% of infected cells. Surviving cells were expanded to 10^8 cells per sublibrary and subjected to another round of infection with *Bb*WT. This process was repeated five times, after which the sensitivity of selected HEK-Cas9 sublibrary cells was assessed using lactate dehydrogenase (LDH) assay. For LDH assay, parental and selected HEK-Cas9 sublibrary A and B cells were seeded at 10^6 per well in a six-well plate in DMEM with 2% (vol/vol) FBS without phenol red indicator. The next day, *Bb* strains were added at the indicated MOI, and infection was allowed to proceed at 37°C and 5% CO_2 for 6 h. The LDH release into cell culture media was determined using CytoTox 96 assay (Cat.No. G1780, Promega) according to the manufacturer's instructions. The percent cytotoxicity was calculated

using the following equation: (OD495 sample – OD495 media)/(OD495 total lysis – OD495 media) × 100.

Cytosolic Fluo-4/AM calcium assay

Cytosolic calcium influx induced by *B. bronchiseptica* infection was assessed through fluorescence intensity measurement and time-lapse imaging using the Fluo-4 Direct Calcium Assay (Cat. No. F10471, Invitrogen), according to the manufacturer's instructions. In brief, 2×10^4 of HeLa cells in DMEM-10%FBS were seeded per well in a 96-well black/clear bottom plate (Corning, USA) or 1×10^4 cells per well in a four-well glass-bottom dish (Cellvis). The next day, cells were loaded with Fluo-4 Direct calcium loading solution supplemented with 5 mM probenecid for 1 h at 37°C and 5% CO_2. *B. bronchiseptica* strains were then added at the indicated MOI in Fluo-4 Direct calcium reagent and either centrifuged onto the HeLa cell surface (5 min, 120 g) or added directly without centrifugation, as indicated. For fluorescence-intensity measurement, a 96-well plate was placed inside the chamber with 37°C and 5% CO_2 of the TecanSpark microplate reader (Tecan, Switzerland), and fluorescence measurements at 494ex/516em with a 10 nm bandwidth for both were taken at 2-min intervals over a period of 10 h. If appropriate, HeLa cells were pre-treated with 2-aminoethyl diphenylborinate (2-APB) at 100 µM for 30 min prior to *B. bronchiseptica* infection. Additionally, glycine at 5 mM was added 5 min before infection when required. For time-lapse imaging, fluorescent signals were captured using a motorized fluorescence microscope (IX-83, Olympus, Japan) equipped with sCMOS camera Photometrics Prime 95B with 30× silicon immersion objective (UPLSAPO30XS, NA = 1.05) at a temperature of 37°C and 5% CO_2 during the imaging process. CellSens software was used for adjustment, image acquisition, and recording sequential images in 16-bit mode at 2-min time intervals. Fluorescence was captured using quadruple dichroic mirror DAPI/FITC/TRITC/CY5 with filter block exc. 555/25 nm, em. 605/52 nm for mScarlet-expressing bacteria, and exc. 490/20 nm, and em. 525/36 nm for Fluo-4/AM.

Visualization of calcium ion fluxes, mitochondrial morphology, and mitochondrial membrane potential and statistics

To examine calcium ion fluxes, a plasmid-encoded red fluorescent Ca^{2+} sensor targeted to either the ER (ER-LAR-Geco) or mitochondria (mito-LAR-Geco) (Table S3) was used in combination with cytosolic Fluo-4/AM calcium assay. Sensor-transfected HeLa cells were seeded on a four-well glass-bottom dish (Cellvis) and loaded with Fluo-4 Direct calcium loading solution supplemented with 5 mM probenecid for 1 h. Infection with *B. bronchiseptica* was performed at a MOI 10:1. Alternatively, mitochondrial morphology or membrane potential was assessed by staining with MitoTracker Orange CM-H2TMRos (MitoTracker, 500 nM, Invitrogen, Cat. No. M7511) or Tetramethylrhodamine (TMRM, 100 nM, Invitrogen, Cat. No. T668) according to the manufacturer's instructions in combination with Fluo-4/AM staining. Fluorescence signals were captured using a motorized fluorescence microscope (IX-83, Olympus, Japan) as described above using 40× dry objective (UPLXAPO40X, NA = 0.95) or 60× oil objective (PLAPON60XOSC2, NA = 1.4) at a temperature 37°C and 5% CO2 during the imaging process. Fluorescence was captured with filter block exc. 555/25 nm, em. 605/52 nm for ER-LAR-Geco, mito-LAR-Geco, MitoTracker, and TMRM, and exc. 490/20 nm, em. 525/36 nm for Fluo-4/AM. Images were collected in a 16-bit format using CellSens software at 3-min time intervals. For quantification of time-lapse imaging, the relative fluorescence intensities (RFI) of regions of interest (ROIs) in cells expressing ER-LAR-Geco, mito-LAR-Geco, or stained with TMRM, were measured over time using ImageJ/Fiji (74). The resulting values were then compared with the corresponding RFI values in defined time points or in uninfected cells using an unpaired two-tailed *t*-test.

Transmission electron microscopy

In total, 5×10^4 HeLa cells were seeded per coverslip in 24-well plates and incubated at 37°C and 5% CO_2. The next day, cells were infected with *Bb*WT and *Bb*Δ*bteA* stains

at MOI 10:1 or left untreated. Added bacteria were centrifugated (5 min, 120 g) onto the cell surface, and samples were fixed 1 h post-infection by 2% glutaraldehyde, 4% paraformaldehyde in 2 mM $CaCl_2$, and 0.1M HEPES pH 7.4 for 2 h. After washing with bi-distilled water, the cells were postfixed in 1% osmium tetroxide, dehydrated with a series of acetone, and embedded in Epon-Durcupan resin (Sigma-Aldrich, St. Louis, MO, USA). The resin was polymerized at 60°C for 72 h. Ultrathin sections (90 nm) were prepared using a Leica EM UC6 ultramicrotome (Leica Microsystems, Wetzlar, Germany) with a diamond knife (Diatome, Biel, Switzerland). The sections were mounted on 200 mesh-size copper grids and examined in a JEOL JEM-1400 Flash transmission electron microscope operated at 80 kV, equipped with a Matataki Flash sCMOS camera (JEOL, Akishima, Tokyo, Japan).

Correlative 3D imaging

In total, 1×10^5 of HeLa cells transiently expressing mitochondria-targeted monomeric hyperfolder YFP fluorescent protein (Table S3) were seeded on the 35 mm gridded glass bottom dish (Mattek, Cat.No. P35G-1.5–14-C-GRD) and incubated at 37°C and 5% CO_2. The next day, HeLa cells were infected with mScarlet-expressing *Bb*WT at MOI 10:1, or left untreated. Added bacteria were centrifugated (5 min, 120 g) onto the cell surface, and samples were fixed 0.5 h post-infection by 2.5% glutaraldehyde and 1% paraformaldehyde in 2 mM $CaCl_2$, 0.1M HEPES pH 7.4 for 1 h. During this fixation period, fluorescence imaging of bacteria and mitochondria was performed using a motorized fluorescence microscope (IX-83, Olympus, Japan) equipped with sCMOS camera Photometrics Prime 95B with 100 × oil-immersion objective (UPLXAPO100XOPH, N.A. = 1.45). Fluorescence was captured using quadruple dichroic mirror DAPI/FITC/TRITC/CY5 with filter block exc. 555/25 nm, em. 605/52 nm for mScarlet, and exc. 490/20 nm, em. 525/36 nm for YFP. Images were collected in a 16-bit format using CellSens software, with Z-stacks taken with 0.26 µm z-steps and deconvolution performed with Advanced Maximum Likelihood (AMLE) filters.

Cells were then washed with 0.1M HEPES (3 × 10 min), post-fixed in reduced 1% osmium tetroxide with 1.5% $K_3(FeCN)_6$, and then in 1% osmium tetroxide (both in 0.1M HEPES, 30 min, RT). Following washing with the 0.1M HEPES buffer, bi-distilled water, and contrasting with 1% uranyl acetate in water (30 min, no light, RT), samples were rinsed again with bi-distilled water and passed through dehydration steps with increasing concentrations of ethanol (30%, 50%, 70%, 95%, and 100%, 2 min each, except 5 min in 100%). Finally, samples were embedded in epoxy Epon-Durcupan resin (Sigma-Aldrich, St. Louis, MO, USA) and polymerized for 72 h at 60°C. All the steps were performed in the 35 mm glass bottom gridded dishes. The small flat epon block was mounted on regular SEM stubs using conductive carbon and coated with 25 nm of platinum using High Vacuum Coater Leica ACE600 (Leica Microsystems, Wetzlar, Germany)

During FIB-SEM imaging, ion milling and image acquisition were performed in a Dual-beam system Tescan Amber Cryo (Tescan Group, Brno, Czech Republic). The target cell was localized by finding the correct coordinates and comparing images from optical microscopy with overview SEM of secondary electrons signal from the top of the resin block (30 kV, 0.8 nA, Everhart–Thornley detector). On the top of the area of interest, a protective layer of platinum (1000 nm) was deposited using a single gas injection system. A large trench around the protective region was milled at a current of 21nA and 30kV by the focus ion beam. It was followed by fine milling at 0.5 nA and 30kV, and the thickness of slices was 10 nm. SEM images were acquired at 2 kV, 0.2 nA, using the Axial BSE detector with a pixel size of 5 nm.

For the FIB-SEM data analysis, the stacks of images were aligned and denoised with a median filter in Amira 3D 2024.1 (Thermo Fisher Scientific) software. The surface of the nucleus and mitochondria were automatically segmented with a pretrained neural network in NIS Elements 6.02.02 (Nikon) software. Correlation with optical microscopy data and data visualization was processed in Amira 3D 2024.1 (Thermo Fisher Scientific) software.

Image processing

All image processing steps were performed using ImageJ/ Fiji (74) or Amira 3D 2024.1. Final images were assembled in Adobe Illustrator (Adobe).

ACKNOWLEDGMENTS

This work was supported by grant 21-05466S of the Czech Science Foundation (www.gacr.cz), grant Talking microbes - understanding microbial interactions within One Health framework (CZ.02.01.01/00/22_008/0004597) of the Ministry of Education, Youth and Sports of the Czech Republic (www.msmt.cz), and the Lumina Queruntur Fellowship LQ200202001 of the Czech Academy of Sciences to J.K. O.C. was funded by ESF International Mobility of Researchers, grant number CZ.02.2.69/0.0/0.0/18_053/0017705. We also acknowledge the support of the project LM2023053 (Czech National Node to the European Infrastructure for Translational Medicine) from the Ministry of Education, Youth and Sports of the Czech Republic, and the Electron Microscopy Core Facility, IMG ASCR, Prague, CR, supported by MEYS CR (LM2018129, LM2023050, CZ.02.1.01/0.0/0.0/18_046/0016045, CZ.02.1.01/0.0/0.0/16_013/0001775), particularly the contributions of Dominik Pinkas. The funders had no role in study design, data collection and analysis, decision to publish, or preparation of the manuscript.

AUTHOR AFFILIATIONS

[1]Laboratory of Infection Biology, Institute of Microbiology, Czech Academy of Sciences, Prague, Czech Republic
[2]Laboratory of Molecular Biology of Bacterial Pathogens, Institute of Microbiology, Czech Academy of Sciences, Prague, Czech Republic
[3]Electron Microscopy Core Facility, Institute of Molecular Genetics, Czech Academy of Sciences, Prague, Czech Republic
[4]Department of Genetics and Microbiology, Faculty of Science, Charles University, Prague, Czech Republic
[5]Laboratory of Cell Signalling, Institute of Microbiology, Czech Academy of Sciences, Prague, Czech Republic

AUTHOR ORCIDs

Jana Kamanova http://orcid.org/0000-0001-6574-4404

FUNDING

Funder	Grant(s)	Author(s)
Grantová Agentura České Republiky (GAČR)	21-05466S	Jana Kamanova
Ministerstvo Školství, Mládeže a Tělovýchovy (MŠMT)	CZ.02.01.01/00/22_008/0004597	Jana Kamanova
Akademie Věd České Republiky (CAS)	LQ200202001	Jana Kamanova
Ministerstvo Školství, Mládeže a Tělovýchovy (MŠMT)	CZ.02.2.69/0.0/0.0/18_053/0017705	Ondrej Cerny

AUTHOR CONTRIBUTIONS

Martin Zmuda, Data curation, Formal analysis, Investigation, Software, Validation, Visualization, Writing – review and editing | Eliska Sedlackova, Formal analysis, Investigation, Validation | Barbora Pravdova, Formal analysis, Investigation | Monika Cizkova, Investigation | Marketa Dalecka, Investigation, Methodology | Ondrej Cerny, Investigation, Methodology, Supervision, Writing – review and editing | Tania Romero Allsop, Formal analysis, Investigation | Tomas Grousl, Methodology, Supervision, Validation

| Ivana Malcova, Methodology | Jana Kamanova, Conceptualization, Data curation, Formal analysis, Funding acquisition, Investigation, Methodology, Project administration, Resources, Supervision, Validation, Visualization, Writing – original draft, Writing – review and editing

DATA AVAILABILITY

The raw sequencing data for the generated HEK-Cas9 A and B sublibraries are available from https://zenodo.org/records/14055612. All additional data are included within the main text and supplemental material.

ADDITIONAL FILES

The following material is available online.

Supplemental Material

Supplemental figures and tables (mBio01925-24-s0001.pdf). Fig. S1 to S10; Tables S1 to S3.
Video legends (mBio01925-24-s0002.docx). Legends for Videos S1 to S8.
Video S1 (mBio01925-24-s0003.avi). Imaging of morphological changes and plasma membrane permeability in HeLa cells.
Video S2 (mBio01925-24-s0004.avi). Calcium imaging.
Video S3 (mBio01925-24-s0005.avi). Calcium imaging.
Video S4 (mBio01925-24-s0006.avi). ER calcium imaging.
Video S5 (mBio01925-24-s0007.avi). Mitochondrial calcium imaging.
Video S6 (mBio01925-24-s0008.avi). Imaging of mitochondria morphology.
Video S7 (mBio01925-24-s0009.avi). Imaging of mitochondrial membrane potential.
Video S8 (mBio01925-24-s0010.avi). Imaging of mitochondrial membrane potential.

REFERENCES

1. Mattoo S, Cherry JD. 2005. Molecular pathogenesis, epidemiology, and clinical manifestations of respiratory infections due to *Bordetella pertussis* and other *Bordetella* subspecies. Clin Microbiol Rev 18:326–382. https://doi.org/10.1128/CMR.18.2.326-382.2005
2. Goodnow RA. 1980. Biology of *Bordetella bronchiseptica*. Microbiol Rev 44:722–738. https://doi.org/10.1128/mr.44.4.722-738.1980
3. Melvin JA, Scheller EV, Miller JF, Cotter PA. 2014. *Bordetella pertussis* pathogenesis: current and future challenges. Nat Rev Microbiol 12:274–288. https://doi.org/10.1038/nrmicro3235
4. Warfel JM, Zimmerman LI, Merkel TJ. 2014. Acellular pertussis vaccines protect against disease but fail to prevent infection and transmission in a nonhuman primate model. Proc Natl Acad Sci USA 111:787–792. https://doi.org/10.1073/pnas.1314688110
5. Althouse BM, Scarpino SV. 2015. Asymptomatic transmission and the resurgence of *Bordetella pertussis*. BMC Med 13:146. https://doi.org/10.1186/s12916-015-0382-8
6. Kapil P, Wang Y, Zimmerman L, Gaykema M, Merkel TJ. 2024. Repeated *Bordetella pertussis* infections are required to reprogram acellular pertussis vaccine-primed host responses in the baboon model. J Infect Dis 229:376–383. https://doi.org/10.1093/infdis/jiad332
7. Taha-Abdelaziz K, Bassel LL, Harness ML, Clark ME, Register KB, Caswell JL. 2016. Cilia-associated bacteria in fatal *Bordetella bronchiseptica* pneumonia of dogs and cats. J Vet Diagn Invest 28:369–376. https://doi.org/10.1177/1040638716646806
8. Chambers JK, Matsumoto I, Shibahara T, Haritani M, Nakayama H, Uchida K. 2019. An outbreak of fatal *Bordetella bronchiseptica* bronchopneumonia in puppies. J Comp Pathol 167:41–45. https://doi.org/10.1016/j.jcpa.2018.12.002
9. Brockmeier SL, Palmer MV, Bolin SR, Rimler RB. 2001. Effects of intranasal inoculation with *Bordetella bronchiseptica*, porcine reproductive and respiratory syndrome virus, or a combination of both organisms on subsequent infection with *Pasteurella multocida* in pigs. Am J Vet Res 62:521–525. https://doi.org/10.2460/ajvr.2001.62.521
10. Jorgensen I, Rayamajhi M, Miao EA. 2017. Programmed cell death as a defence against infection. Nat Rev Immunol 17:151–164. https://doi.org/10.1038/nri.2016.147
11. Ashida H, Mimuro H, Ogawa M, Kobayashi T, Sanada T, Kim M, Sasakawa C. 2011. Cell death and infection: a double-edged sword for host and pathogen survival. J Cell Biol 195:931–942. https://doi.org/10.1083/jcb.201108081
12. Goldman WE, Cookson BT. 1988. Structure and functions of the *Bordetella* tracheal cytotoxin. Tokai J Exp Clin Med 13 Suppl:187–191.
13. Kessie DK, Lodes N, Oberwinkler H, Goldman WE, Walles T, Steinke M, Gross R. 2020. Activity of tracheal cytotoxin of *Bordetella pertussis* in a human tracheobronchial 3D tissue model. Front Cell Infect Microbiol 10:614994. https://doi.org/10.3389/fcimb.2020.614994
14. Khelef N, Zychlinsky A, Guiso N. 1993. *Bordetella pertussis* induces apoptosis in macrophages: role of adenylate cyclase-hemolysin. Infect Immun 61:4064–4071. https://doi.org/10.1128/iai.61.10.4064-4071.1993
15. Ahmad JN, Cerny O, Linhartova I, Masin J, Osicka R, Sebo P. 2016. cAMP signalling of *Bordetella* adenylate cyclase toxin through the SHP-1 phosphatase activates the BimEL-Bax pro-apoptotic cascade in phagocytes. Cell Microbiol 18:384–398. https://doi.org/10.1111/cmi.12519
16. Stockbauer KE, Foreman-Wykert AK, Miller JF. 2003. *Bordetella* type III secretion induces caspase 1-independent necrosis. Cell Microbiol 5:123–132. https://doi.org/10.1046/j.1462-5822.2003.00260.x
17. Panina EM, Mattoo S, Griffith N, Kozak NA, Yuk MH, Miller JF. 2005. A genome-wide screen identifies a *Bordetella* type III secretion effector and candidate effectors in other species. Mol Microbiol 58:267–279. https://doi.org/10.1111/j.1365-2958.2005.04823.x
18. Kamanova J. 2020. *Bordetella* type III secretion injectosome and effector proteins. Front Cell Infect Microbiol 10:466. https://doi.org/10.3389/fcimb.2020.00466

19. Yuk MH, Harvill ET, Miller JF. 1998. The BvgAS virulence control system regulates type III secretion in *Bordetella bronchiseptica*. Mol Microbiol 28:945–959. https://doi.org/10.1046/j.1365-2958.1998.00850.x
20. Pilione MR, Harvill ET. 2006. The *Bordetella bronchiseptica* type III secretion system inhibits gamma interferon production that is required for efficient antibody-mediated bacterial clearance. Infect Immun 74:1043–1049. https://doi.org/10.1128/IAI.74.2.1043-1049.2006
21. Nicholson TL, Brockmeier SL, Loving CL, Register KB, Kehrli ME, Shore SM. 2014. The *Bordetella bronchiseptica* type III secretion system is required for persistence and disease severity but not transmission in swine. Infect Immun 82:1092–1103. https://doi.org/10.1128/IAI.01115-13
22. Cotter PA, Miller JF. 1994. BvgAS-mediated signal transduction: analysis of phase-locked regulatory mutants of *Bordetella bronchiseptica* in a rabbit model. Infect Immun 62:3381–3390. https://doi.org/10.1128/iai.62.8.3381-3390.1994
23. Buboltz AM, Nicholson TL, Weyrich LS, Harvill ET. 2009. Role of the type III secretion system in a hypervirulent lineage of *Bordetella bronchiseptica*. Infect Immun 77:3969–3977. https://doi.org/10.1128/IAI.01362-08
24. Ahuja U, Liu M, Tomida S, Park J, Souda P, Whitelegge J, Li H, Harvill ET, Parkhill J, Miller JF. 2012. Phenotypic and genomic analysis of hypervirulent human-associated *Bordetella bronchiseptica*. BMC Microbiol 12:167. https://doi.org/10.1186/1471-2180-12-167
25. Bayram J, Malcova I, Sinkovec L, Holubova J, Streparola G, Jurnecka D, Kucera J, Sedlacek R, Sebo P, Kamanova J. 2020. Cytotoxicity of the effector protein BteA was attenuated in *Bordetella pertussis* by insertion of an alanine residue. PLoS Pathog 16:e1008512. https://doi.org/10.1371/journal.ppat.1008512
26. French CT, Panina EM, Yeh SH, Griffith N, Arambula DG, Miller JF. 2009. The *Bordetella* type III secretion system effector BteA contains a conserved N-terminal motif that guides bacterial virulence factors to lipid rafts. Cell Microbiol 11:1735–1749. https://doi.org/10.1111/j.1462-5822.2009.01361.x
27. Geissler B. 2012. Bacterial toxin effector-membrane targeting: outside in, then back again. Front Cell Infect Microbiol 2:75. https://doi.org/10.3389/fcimb.2012.00075
28. Yahalom A, Davidov G, Kolusheva S, Shaked H, Barber-Zucker S, Zarivach R, Chill JH. 2019. Structure and membrane-targeting of a *Bordetella pertussis* effector N-terminal domain. Biochim Biophys Acta 1861:183054. https://doi.org/10.1016/j.bbamem.2019.183054
29. Malcova I, Bumba L, Uljanic F, Kuzmenko D, Nedomova J, Kamanova J. 2021. Lipid binding by the N-terminal motif mediates plasma membrane localization of *Bordetella* effector protein BteA. J Biol Chem 296:100607. https://doi.org/10.1016/j.jbc.2021.100607
30. Kuwae A, Momose F, Nagamatsu K, Suyama Y, Abe A. 2016. BteA secreted from the *Bordetella bronchiseptica* type III secetion system induces necrosis through an actin cytoskeleton signaling pathway and inhibits phagocytosis by macrophages. PLoS One 11:e0148387. https://doi.org/10.1371/journal.pone.0148387
31. Chertkova AO, Mastop M, Postma M, Bommel N, Niet S, Batenburg KL, Joosen L, Gadella TWJ, Okada Y, Goedhart J. 2020. Robust and bright genetically encoded fluorescent markers for highlighting structures and compartments in mammalian cells. bioRxiv. https://doi.org/10.1101/160374
32. Chang S-J, Jin SC, Jiao X, Galán JE. 2019. Unique features in the intracellular transport of typhoid toxin revealed by a genome-wide screen. PLoS Pathog 15:e1007704. https://doi.org/10.1371/journal.ppat.1007704
33. Blondel CJ, Park JS, Hubbard TP, Pacheco AR, Kuehl CJ, Walsh MJ, Davis BM, Gewurz BE, Doench JG, Waldor MK. 2016. CRISPR/Cas9 screens reveal requirements for host cell sulfation and fucosylation in bacterial type III secretion system-mediated cytotoxicity. Cell Host Microbe 20:226–237. https://doi.org/10.1016/j.chom.2016.06.010
34. Shahi I, Llaneras CN, Perelman SS, Torres VJ, Ratner AJ. 2022. Genome-wide CRISPR-Cas9 screen does not identify host factors modulating *Streptococcus agalactiae* β-hemolysin/cytolysin-induced cell death. Microbiol Spectr 10:e0218621. https://doi.org/10.1128/spectrum.02186-21
35. Sanjana NE, Shalem O, Zhang F. 2014. Improved vectors and genome-wide libraries for CRISPR screening. Nat Methods 11:783–784. https://doi.org/10.1038/nmeth.3047
36. Subramanian K, Meyer T. 1997. Calcium-induced restructuring of nuclear envelope and endoplasmic reticulum calcium stores. Cell 89:963–971. https://doi.org/10.1016/s0092-8674(00)80281-0
37. Horn A, Raavicharla S, Shah S, Cox D, Jaiswal JK. 2020. Mitochondrial fragmentation enables localized signaling required for cell repair. J Cell Biol 219:e201909154. https://doi.org/10.1083/jcb.201909154
38. Gee KR, Brown KA, Chen WN, Bishop-Stewart J, Gray D, Johnson I. 2000. Chemical and physiological characterization of fluo-4 Ca^{2+}-indicator dyes. Cell Calcium 27:97–106. https://doi.org/10.1054/ceca.1999.0095
39. Wu J, Prole DL, Shen Y, Lin Z, Gnanasekaran A, Liu Y, Chen L, Zhou H, Chen SRW, Usachev YM, Taylor CW, Campbell RE. 2014. Red fluorescent genetically encoded Ca^{2+} indicators for use in mitochondria and endoplasmic reticulum. Biochem J 464:13–22. https://doi.org/10.1042/BJ20140931
40. Rizzuto R, De Stefani D, Raffaello A, Mammucari C. 2012. Mitochondria as sensors and regulators of calcium signalling. Nat Rev Mol Cell Biol 13:566–578. https://doi.org/10.1038/nrm3412
41. Rasola A, Bernardi P. 2011. Mitochondrial permeability transition in Ca^{2+}-dependent apoptosis and necrosis. Cell Calcium 50:222–233. https://doi.org/10.1016/j.ceca.2011.04.007
42. Kuwae A, Matsuzawa T, Ishikawa N, Abe H, Nonaka T, Fukuda H, Imajoh-Ohmi S, Abe A. 2006. BopC is a novel type III effector secreted by *Bordetella bronchiseptica* and has a critical role in type III-dependent necrotic cell death. J Biol Chem 281:6589–6600. https://doi.org/10.1074/jbc.M512711200
43. Kuwae A, Ohishi M, Watanabe M, Nagai M, Abe A. 2003. BopB is a type III secreted protein in *Bordetella bronchiseptica* and is required for cytotoxicity against cultured mammalian cells. Cell Microbiol 5:973–983. https://doi.org/10.1046/j.1462-5822.2003.00341.x
44. Bedoui S, Herold MJ, Strasser A. 2020. Emerging connectivity of programmed cell death pathways and its physiological implications. Nat Rev Mol Cell Biol 21:678–695. https://doi.org/10.1038/s41580-020-0270-8
45. Barros LF, Kanaseki T, Sabirov R, Morishima S, Castro J, Bittner CX, Maeno E, Ando-Akatsuka Y, Okada Y. 2003. Apoptotic and necrotic blebs in epithelial cells display similar neck diameters but different kinase dependency. Cell Death Differ 10:687–697. https://doi.org/10.1038/sj.cdd.4401236
46. Dong Z, Saikumar P, Weinberg JM, Venkatachalam MA. 2006. Calcium in cell injury and death. Annu Rev Pathol 1:405–434. https://doi.org/10.1146/annurev.pathol.1.110304.100218
47. Trump BF, Berezesky IK. 1995. Calcium-mediated cell injury and cell death. FASEB J 9:219–228. https://doi.org/10.1096/fasebj.9.2.7781924
48. Yin HL, Albrecht JH, Fattoum A. 1981. Identification of gelsolin, a Ca^{2+}-dependent regulatory protein of actin gel-sol transformation, and its intracellular distribution in a variety of cells and tissues. J Cell Biol 91:901–906. https://doi.org/10.1083/jcb.91.3.901
49. Wales P, Schuberth CE, Aufschnaiter R, Fels J, García-Aguilar I, Janning A, Dlugos CP, Schäfer-Herte M, Klingner C, Wälte M, Kuhlmann J, Menis E, Hockaday Kang L, Maier KC, Hou W, Russo A, Higgs HN, Pavenstädt H, Vogl T, Roth J, Qualmann B, Kessels MM, Martin DE, Mulder B, Wedlich-Söldner R. 2016. Calcium-mediated actin reset (CaAR) mediates acute cell adaptations. Elife 5:e19850. https://doi.org/10.7554/eLife.19850
50. Aoki K, Harada S, Kawaji K, Matsuzawa K, Uchida S, Ikenouchi J. 2021. STIM-Orai1 signaling regulates fluidity of cytoplasm during membrane blebbing. Nat Commun 12:480. https://doi.org/10.1038/s41467-020-20826-5
51. Weber H, Hühns S, Lüthen F, Jonas L. 2009. Calpain-mediated breakdown of cytoskeletal proteins contributes to cholecystokinin-induced damage of rat pancreatic acini. Int J Exp Pathol 90:387–399. https://doi.org/10.1111/j.1365-2613.2009.00638.x
52. Rami A. 2003. Ischemic neuronal death in the rat hippocampus: the calpain-calpastatin-caspase hypothesis. Neurobiol Dis 13:75–88. https://doi.org/10.1016/s0969-9961(03)00018-4
53. Okuda A, Furuya K, Kiyohara T. 2003. ATP-induced calcium oscillations and change of P2Y subtypes with culture conditions in HeLa cells. Cell Biochem Funct 21:61–68. https://doi.org/10.1002/cbf.992
54. Jumper J, Evans R, Pritzel A, Green T, Figurnov M, Ronneberger O, Tunyasuvunakool K, Bates R, Žídek A, Potapenko A, et al. 2021. Highly accurate protein structure prediction with AlphaFold. Nature New Biol 596:583–589. https://doi.org/10.1038/s41586-021-03819-2

55. Hallgren J, Tsirigos KD, Pedersen MD, Almagro Armenteros JJ, Marcatili P, Nielsen H, Krogh A, Winther O. 2022. DeepTMHMM predicts alpha and beta transmembrane proteins using deep neural networks. bioRxiv. https://doi.org/10.1101/2022.04.08.487609
56. Nogawa H, Kuwae A, Matsuzawa T, Abe A. 2004. The type III secreted protein BopD in *Bordetella bronchiseptica* is complexed with BopB for pore formation on the host plasma membrane. J Bacteriol 186:3806–3813. https://doi.org/10.1128/JB.186.12.3806-3813.2004
57. Medhekar B, Shrivastava R, Mattoo S, Gingery M, Miller JF. 2009. Bordetella Bsp22 forms a filamentous type III secretion system tip complex and is immunoprotective *in vitro* and *in vivo*. Mol Microbiol 71:492–504. https://doi.org/10.1111/j.1365-2958.2008.06543.x
58. Navarrete KM, Bumba L, Prudnikova T, Malcova I, Allsop TR, Sebo P, Kamanova J. 2023. BopN is a gatekeeper of the *Bordetella* type III secretion system. Microbiol Spectr 11:e0411222. https://doi.org/10.1128/spectrum.04112-22
59. Heidersbach AJ, Dorighi KM, Gomez JA, Jacobi AM, Haley B. 2023. A versatile, high-efficiency platform for CRISPR-based gene activation. Nat Commun 14:902. https://doi.org/10.1038/s41467-023-36452-w
60. Raffaello A, Mammucari C, Gherardi G, Rizzuto R. 2016. Calcium at the center of cell signaling: interplay between endoplasmic reticulum, mitochondria, and lysosomes. Trends Biochem Sci 41:1035–1049. https://doi.org/10.1016/j.tibs.2016.09.001
61. Bagur R, Hajnóczky G. 2017. Intracellular Ca^{2+} sensing: its role in calcium homeostasis and signaling. Mol Cell 66:780–788. https://doi.org/10.1016/j.molcel.2017.05.028
62. Loncke J, Kaasik A, Bezprozvanny I, Parys JB, Kerkhofs M, Bultynck G. 2021. Balancing ER-mitochondrial Ca^{2+} fluxes in health and disease. Trends Cell Biol 31:598–612. https://doi.org/10.1016/j.tcb.2021.02.003
63. Bartok A, Weaver D, Golenár T, Nichtova Z, Katona M, Bánsághi S, Alzayady KJ, Thomas VK, Ando H, Mikoshiba K, Joseph SK, Yule DI, Csordás G, Hajnóczky G. 2019. IP_3 receptor isoforms differently regulate ER-mitochondrial contacts and local calcium transfer. Nat Commun 10:3726. https://doi.org/10.1038/s41467-019-11646-3
64. Maruyama T, Kanaji T, Nakade S, Kanno T, Mikoshiba K. 1997. 2APB, 2-aminoethoxydiphenyl borate, a membrane-penetrable modulator of Ins(1,4,5)P_3-induced Ca^{2+} release. J Biochem 122:498–505. https://doi.org/10.1093/oxfordjournals.jbchem.a021780
65. Prakriya M, Lewis RS. 2001. Potentiation and inhibition of Ca^{2+} release-activated Ca^{2+} channels by 2-aminoethyldiphenyl borate (2-APB) occurs independently of IP_3 receptors. J Physiol 536:3–19. https://doi.org/10.1111/j.1469-7793.2001.t01-1-00003.x
66. Lievremont JP, Bird GS, Putney JW Jr. 2005. Mechanism of inhibition of TRPC cation channels by 2-aminoethoxydiphenylborane. Mol Pharmacol 68:758–762. https://doi.org/10.1124/mol.105.012856
67. Chokshi R, Fruasaha P, Kozak JA. 2012. 2-aminoethyl diphenyl borinate (2-APB) inhibits TRPM7 channels through an intracellular acidification mechanism. Channels (Austin) 6:362–369. https://doi.org/10.4161/chan.21628
68. Giorgi C, Marchi S, Pinton P. 2018. The machineries, regulation and cellular functions of mitochondrial calcium. Nat Rev Mol Cell Biol 19:713–730. https://doi.org/10.1038/s41580-018-0052-8
69. Giorgio V, Burchell V, Schiavone M, Bassot C, Minervini G, Petronilli V, Argenton F, Forte M, Tosatto S, Lippe G, Bernardi P. 2017. Ca^{2+} binding to F-ATP synthase β subunit triggers the mitochondrial permeability transition. EMBO Rep 18:1065–1076. https://doi.org/10.15252/embr.201643354
70. Kim JS, He L, Lemasters JJ. 2003. Mitochondrial permeability transition: a common pathway to necrosis and apoptosis. Biochem Biophys Res Commun 304:463–470. https://doi.org/10.1016/s0006-291x(03)00618-1
71. Bernardi P, Gerle C, Halestrap AP, Jonas EA, Karch J, Mnatsakanyan N, Pavlov E, Sheu SS, Soukas AA. 2023. Identity, structure, and function of the mitochondrial permeability transition pore: controversies, consensus, recent advances, and future directions. Cell Death Differ 30:1869–1885. https://doi.org/10.1038/s41418-023-01187-0
72. Gibson DG, Young L, Chuang R-Y, Venter JC, Hutchison CA 3rd, Smith HO. 2009. Enzymatic assembly of DNA molecules up to several hundred kilobases. Nat Methods 6:343–345. https://doi.org/10.1038/nmeth.1318
73. Joung J, Konermann S, Gootenberg JS, Abudayyeh OO, Platt RJ, Brigham MD, Sanjana NE, Zhang F. 2017. Genome-scale CRISPR-Cas9 knockout and transcriptional activation screening. Nat Protoc 12:828–863. https://doi.org/10.1038/nprot.2017.016
74. Schindelin J, Arganda-Carreras I, Frise E, Kaynig V, Longair M, Pietzsch T, Preibisch S, Rueden C, Saalfeld S, Schmid B, Tinevez JY, White DJ, Hartenstein V, Eliceiri K, Tomancak P, Cardona A. 2012. Fiji: an open-source platform for biological-image analysis. Nat Methods 9:676–682. https://doi.org/10.1038/nmeth.2019